Articles
doi.org/10.1002/batt.202100113

Chemistry Europe
European Chemical Societies Publishing

Hygroscopic Double-Layer Gel Polymer Electrolyte toward High-Performance Low-Temperature Zinc Hybrid Batteries

Changyuan Yan,[a] Yangyang Wang,[a] Zixuan Chen,[a] and Xianyu Deng*[a]

Aqueous zinc hybrid batteries have been rapidly developed to overcome the sluggish kinetics of divalent zinc ions in the cathode of Zn-based batteries. However, their cycle life is limited by water decomposition during the operation, specifically at low current rate for long-term cycles. Herein, we propose a zinc hybrid battery with excellent adaptability of low-temperature, at which the water decomposition is seriously restrained. The battery involves a hygroscopic double-layer gel polymer electrolyte, in which one layer close to the $LiFePO_4$ cathode provides Li^+, and the other layer close to the Zn anode provides Zn^{2+}. The use of the double-layer electrolyte can both weaken the water reactivity and increase the salt concentration, leading to a high-performance of the batteries. It enables the hybrid batteries to operate at −20 °C and achieve stability for over 300 cycles with a capacity retention of 85.14% and Coulombic efficiency of ~100% at a low current rate of 85 mA g^{-1}. Moreover, the spontaneous hygroscopic system, opposite to that of "water-in-salt", can efficiently reduce manufacturing costs and improve ionic conductivity. This provides an advanced pathway for designing electrolytes to achieve high-performance and low-cost batteries with excellent adaptability of low-temperature.

1. Introduction

With the fast development of rechargeable batteries in energy storage systems, the applications of the batteries have been continuously increasing in various fields, including consumer electronics, electric vehicles, drones, and even small satellites.[1–4] High capability, safety, flexibility and light-weight become the main aims in future batteries. Aqueous rechargeable zinc batteries, have been reported with several advantages, such as non-flammability, environmental friendliness, and suitable energy density.[5–8] Nevertheless, the development of aqueous batteries remains restricted due to water-driven parasitic reactions[9–11] and the inherent low freezing point of water molecules.[12] These parasitic reactions, including the undesirable hydrogen evolution reaction (HER) and oxygen evolution reaction (OER), occur over the long-term operation of the battery due to high reactivity of numerous water molecules. This is detrimental to the anode and cathode materials, for the following reactions. First, OH^- generated by water decomposition will promote the formation of a passivating layer on the Zn surface (such as ZnO, $Zn(OH)_2$ and zincate).[13,14] This inevitably increases the interface impedance between the electrode and electrolyte, thereby hindering ion conduction. Second, OH^- and O_2 in the cathode induce the dissolution of active material and further accelerate the loss of capacity.[15,16]

Additionally, conventional aqueous electrolyte freezes at subzero temperatures due to hydrogen bonds (H-bonds) present among water molecules, which severely restricts ion migration and causes battery failure. In many northern countries, such as the northeastern of China, the temperature remains below 0 °C for nearly five months of the year. This environmental factor specifically manifests the importance of low-temperature adaptability for rechargeable aqueous batteries. These issues can be addressed by adding salt to the electrolytes to effectively increase ion hydration, producing fewer side reactions[17,18] and a lower freezing point.[19–21] This method was derived from the "water-in-salt" electrolytes using highly concentrated salts.[22] However, solutions with high salt concentration will precipitate out at low temperatures, causing the electrolyte to crystallize. Meanwhile, the problem of high manufacturing costs still exists. Additionally, when a "water-in-salt" electrolyte is applied at low temperatures, the electrolyte state, whether a liquid or not, must first be considered. However, only liquid $ZnCl_2$ solution can reach 10 m (m represents molar concentration (mol kg^{-1}) at −70 °C,[19,23] which means that the application of other zinc salts is significantly greatly limited at low temperatures. Therefore, simply using the "water-in-salt" strategy for battery operation at low temperatures is usually not a satisfactory choice.

The transport of Zn^{2+} is slow in the host material due to its high charge density causing greater electrostatic interaction with the matrix lattice.[24] For this reason, the zinc hybrid battery has been proposed and studied since 2012.[25] This working mechanism is converted from the single ion transport of the "rocking chair" battery into double ion transport, which well compensates the sluggish diffusion of Zn^{2+}[26] and supports the utilization of a double-layer electrolyte. However, there are few existing studies that report the comparison of the long-term cycle performance of aqueous electrolytes based zinc hybrid batteries at low temperatures and room temperature. For instance, Wang et al. assembled a $Zn/LiMn_2O_4$ hybrid battery based on a dilute electrolyte (1 m $Zn(TFSI)_2$ + 5 m

[a] C. Yan, Dr. Y. Wang, Z. Chen, Prof. X. Deng
Shenzhen Key Laboratory of Advanced Materials
School of Materials Science and Engineering
Harbin Institute of Technology
518055 Shenzhen, China
E-mail: xydeng@hit.edu.cn

Supporting information for this article is available on the WWW under https://doi.org/10.1002/batt.202100113

LiTFSI), where the capacity dropped to zero after 25 cycles at room temperature; however, they have not yet reported the cycle performance at low temperatures.[17] Zhu et al. applied a polyacrylamide (PAM) hydrogel electrolyte containing 2 M $ZnSO_4$ and 4 M LiCl to a Zn/$LiFePO_4$ hybrid battery and exhibited excellent capacity retention at −20 °C. They reported the rate performance for short-term cycles at room temperature, without the discussion of the capacity retention after cycling.[20] Therefore, the vital role of water molecules at low temperatures is still not confirmed.

Here, to reduce the water molecule activity and high costs caused by a high salt concentration, we designed a hygroscopic double-layer polyethylene glycol (PEG)/bacterial cellulose (BC) electrolyte in a Zn/$LiFePO_4$ hybrid battery through a reverse method to the "water-in-salt" process. Ultra-thin BC hydrogel with an excellent tensile strength (18.16 MPa) was prepared by the freezing–thawing method. The PEG, which is capable of ion migration, was introduced by replacing the water in the BC hydrogel. Without external stimulation, this design completely utilizes the spontaneous water absorption of $Zn(OTf)_2$, LiTFSI, and PEG to improve the ionic conductivity of the gel electrolyte. BC hydrogel electrolytes with different salts and concentrations are also investigated. The low-temperature environment can inhibit the decomposition of the adsorbed water to achieve excellent capacity retention. Furthermore, the hybrid battery with this hygroscopic electrolyte delivers a Coulombic efficiency of approximately 100% and capacity retention of 85.14% after 300 cycles (85 mA g^{-1}) at −20 °C.

2. Results and Discussion

2.1. Preparation and Characterization of the BC Hydrogel

BC is an abundant and renewable natural polymer. Purified cellulose hydrogels with remarkable mechanical properties are easy to obtain, owing to their large aspect ratio and abundant hydroxyl groups.[27,28] However, purified BC hydrogel contains a large amount of water and has a relatively thick thickness, which is not advantageous to battery assembly and energy density.[29] To mitigate this disadvantage, a simple freezing–thawing method was introduced, as shown in Figure 1a. The thickness of the frozen–thawed BC hydrogel decreased to 138 μm, which is much thinner than that of the pristine BC hydrogel (766 μm). Compared with pristine BC hydrogel, frozen–thawed BC hydrogel exhibits lower transparency, which is primarily because of its denser structure and smaller pore size (Figure 1c, d), as discussed later. Meanwhile, the 3D porous structure plays a key role in promoting ion transport. The Brunauer–Emmett–Teller (BET) surface area and pore size distribution were determined by an N_2 adsorption–desorption system (Figure S1a, b, Supporting Information). Notably, the frozen–thawed BC aerogel provides a lower BET surface area of 43.7 $m^2 g^{-1}$ compared to the pristine BC aerogel (56.2 $m^2 g^{-1}$) and exhibits type-IV sorption isotherm curves because of a hysteresis loop at low pressure and fast N_2 adsorption at high pressure. Moreover, the pore size, calculated using the Barrett–Joyner–Halenda (BJH) method, mainly shows a distribution in the mesoporous region (< 50 nm). Figure S1c (Supporting Information) shows that the crystallinity of the frozen–thawed

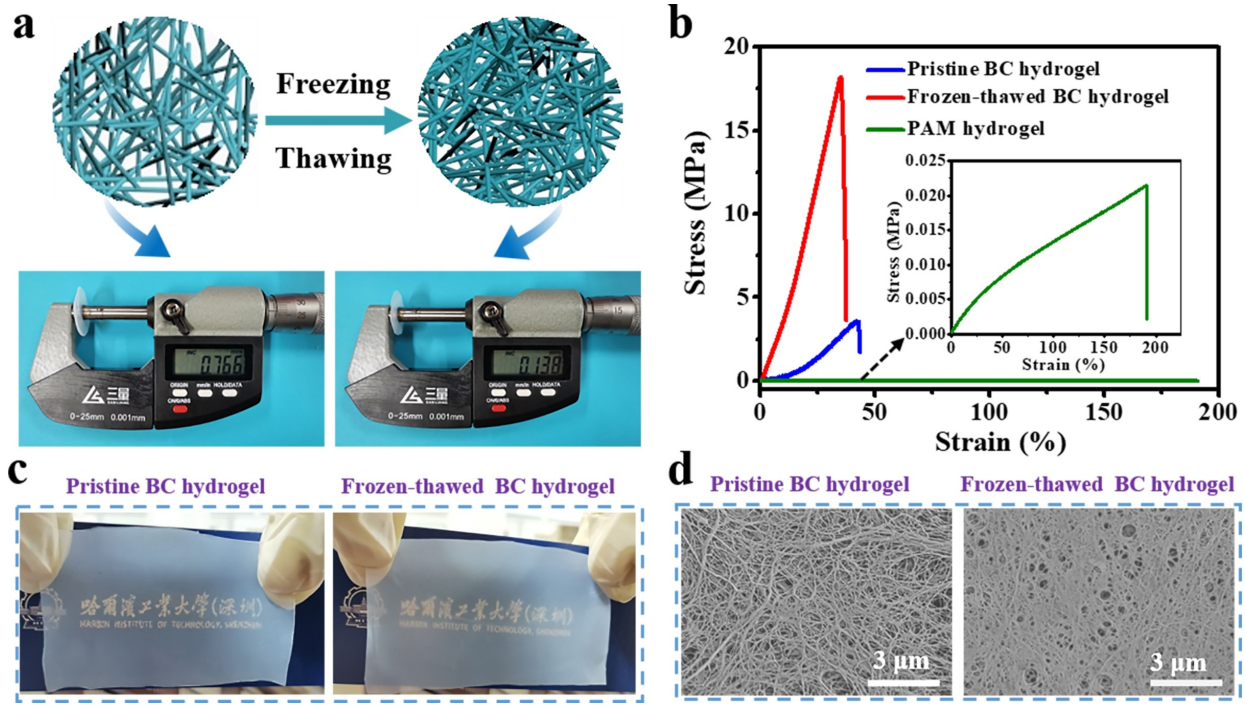

Figure 1. Preparation and characterization of the BC hydrogel. a) Schematic of the synthesis route to BC hydrogel. b) Stress–strain curves of BC hydrogel and PAM hydrogel. c) Photographs and d) SEM images of pristine BC hydrogel and frozen–thawed BC hydrogel.

BC hydrogel on the crystal plane (002) is observed to be significantly enhanced, with a calculated crystallinity of 78.50%.[30] This phenomenon of enhanced crystallinity at low temperatures is similar to polyvinyl alcohol.[31] Electrolytes must have sufficient mechanical properties to inhibit the growth of dendrites while ensuring battery integrity. As expected, the increase in crystallinity substantially improved the mechanical properties of the hydrogel. After thawing, the tensile strength of the BC hydrogel quickly increased from 3.55 MPa to 18.16 MPa, which are nearly three orders of magnitude higher than that of the traditional PAM hydrogel (21.5 KPa, Figure 1b).

2.2. Highly Cyclic Stability of Zn/$LiFePO_4$ Batteries Based on a Hygroscopic Double-Layer Gel Polymer Electrolyte at Low Temperatures

Optical images of mixed acetonitrile solutions of $Zn(OTf)_2$ and LiTFSI and their separate solutions are demonstrated in Figure S2 (Supporting Information). These images reveal that the separate $Zn(OTf)_2$ and LiTFSI acetonitrile solutions were transparent, but that there were precipitates in the mixed solutions with the same concentration. Considering that high salt concentrations can exhibit superior cycle stability and low temperature resistance,[32–34] separated acetonitrile solutions with a respectively high concentration (1.5 M $Zn(OTf)_2$ and 3 M LiTFSI) were adopted to prepare a double-layer electrolyte. The BC/PEG gel electrolyte was then prepared by immersing the PEG-infused BC gel in this salt solution and removing the acetonitrile by vacuum drying. As demonstrated in Figure 2a, the first and second layers comprised the electrolyte containing $Zn(OTf)_2$, which only contacted the Zn anode, and that containing LiTFSI, which only contacted the $LiFePO_4$ cathode, respectively. In general, $Zn(OTf)_2$, LiTFSI, and PEG will absorb water in the air. Combining the above advantages, the double-layer BC/PEG gel electrolyte was placed in a constant temperature and humidity environment to allow it to absorb water spontaneously,[35] the water uptake of the prepared double-layer electrolyte was about 9.05 wt.% (Table S1, Supporting Information).

The hygroscopic BC/PEG electrolyte integrates their respective merits to promote Zn^{2+} and Li^+ transportation (Figure 2b). First, the movement of the PEG segments drives the migration of Zn^{2+} and Li^+ coordinated with the ether bond of PEG.[36,37] Meanwhile, the hydroxyl groups of the BC form H-bonds with the anions (OTf^- and $TFSI^-$), which promotes the dissociation of $Zn(OTf)_2$ and LiTFSI.[38] Second, the part of Zn^{2+} and Li^+ are separated from the coordination of the PEG and converted into $[Zn(H_2O)_6]^{2+}$ and $[Li(H_2O)_4]^+$ by interacting with the surrounding water molecules. These hydrated ions can then promote

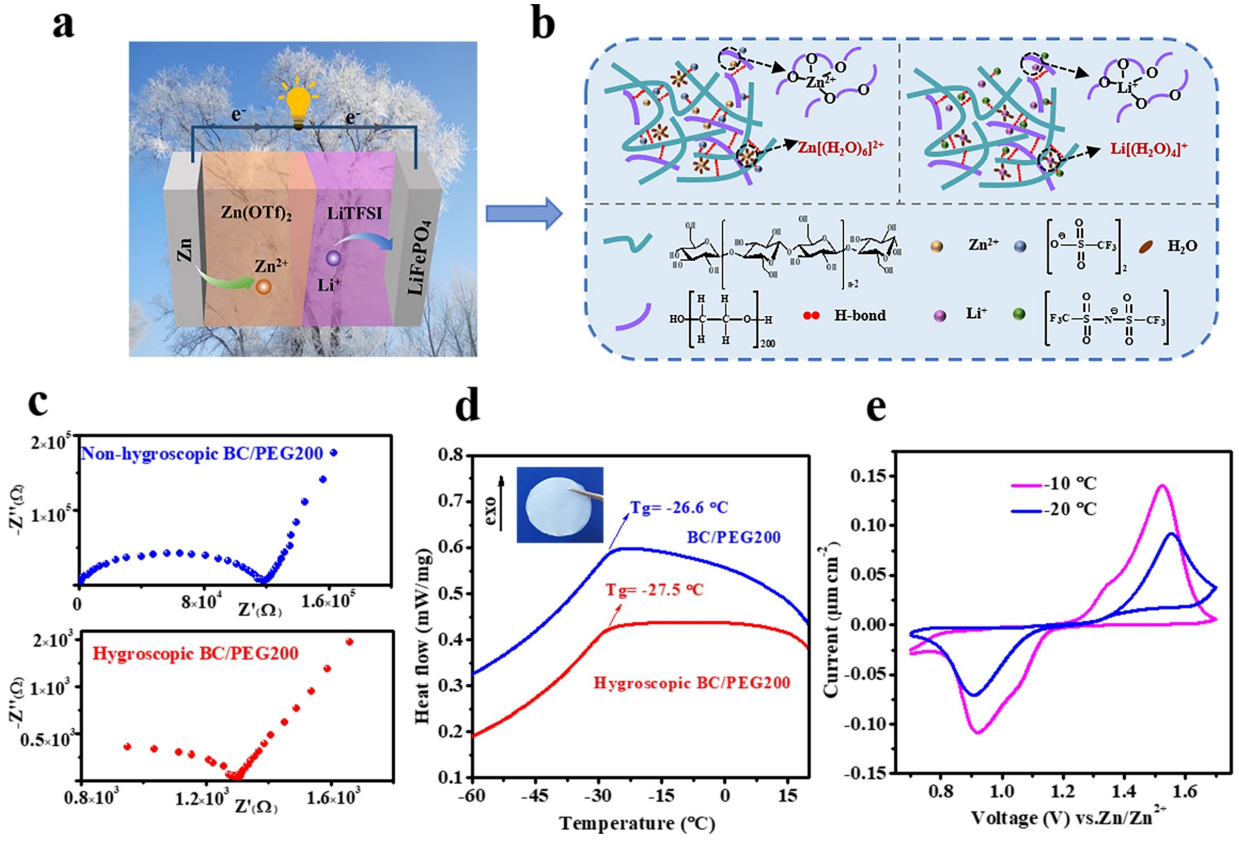

Figure 2. The structure and performances of a hygroscopic double-layer gel polymer electrolyte. Schematic illustration of a) the structure and b) bonding mechanism of hygroscopic double-layer gel polymer electrolyte. c) Nyquist plots of the SS/SS symmetric system based on the non-hygroscopic and hygroscopic BC/PEG200 electrolyte measured at −20 °C. d) DSC curves of the hygroscopic BC/PEG200 electrolyte. e) CV curves of Zn/$LiFePO_4$ at a scan rate of 0.1 mV s^{-1}.

the rapid transport of ions.[22,23] Compared to −10 °C (Figure S3, Supporting Information), the non-hygroscopic gel electrolyte with a high salt concentration has a higher impedance at −20 °C (Figure 2c), making the battery impossible to operate, despite a lower glass transition temperature based on the contribution of PEG200 (Figure 2d). However, after the electrolyte absorbed water, its impedance quickly decreased from 1.2×10^5 Ω to 1.3×10^3 Ω. Additionally, at −20 °C, the hygroscopic electrolyte maintained an ionic conductivity of 0.012 mS cm^{-1}, proving that it can conduct ion transport at −20 °C. Therefore, we assembled a Zn/LiFePO$_4$ battery with the prepared hygroscopic electrolyte for performance evaluation. Figure 2e presents the cyclic voltammetry (CV) curves of the full battery at −10 °C and −20 °C. The CV curve at −20 °C displays that although the current at the peak was significantly reduced, a highly reversible redox peak can still be observed.

The charge–discharge curves (Figure 3a, b) show that the discharge specific capacities at −10 °C and −20 °C were essentially keep stable after 200 cycles, which are 69.5 and 49.3 mAh g^{-1}, respectively. Additionally, the specific capacity decreases slightly after 300 cycles. Figure 3c shows the C-rate performance of the full battery at low temperatures. The specific capacity decreased with the increase of current density due to the kinetic limitations at low temperatures. In addition, although the capacity decayed rapidly at a high current density, at −20 °C, the capacity could be restored to the original value at low current density (17 mA g^{-1}). When PEG300 and PEG400 were employed to prepare the gel electrolyte, the glass transition temperatures (−27.5 °C) of the corresponding hygroscopic electrolytes was the same as that of PEG200 (Figure S4, Supporting Information), which may be caused by the high salt concentration. A single battery with an open circuit voltage (OCV) of 1.162 V is consistent with the theoretical value ~1.172 V.[25] The cycle life of the zinc hybrid battery in this study was evaluated at 85 mA g^{-1}, as shown in Figure 3d. At −10 °C, the battery displayed an initial discharge specific capacity of 69.5 mAh g^{-1} with a capacity retention of 82.39% after 300 cycles. At −20 °C, it exhibited a specific capacity of

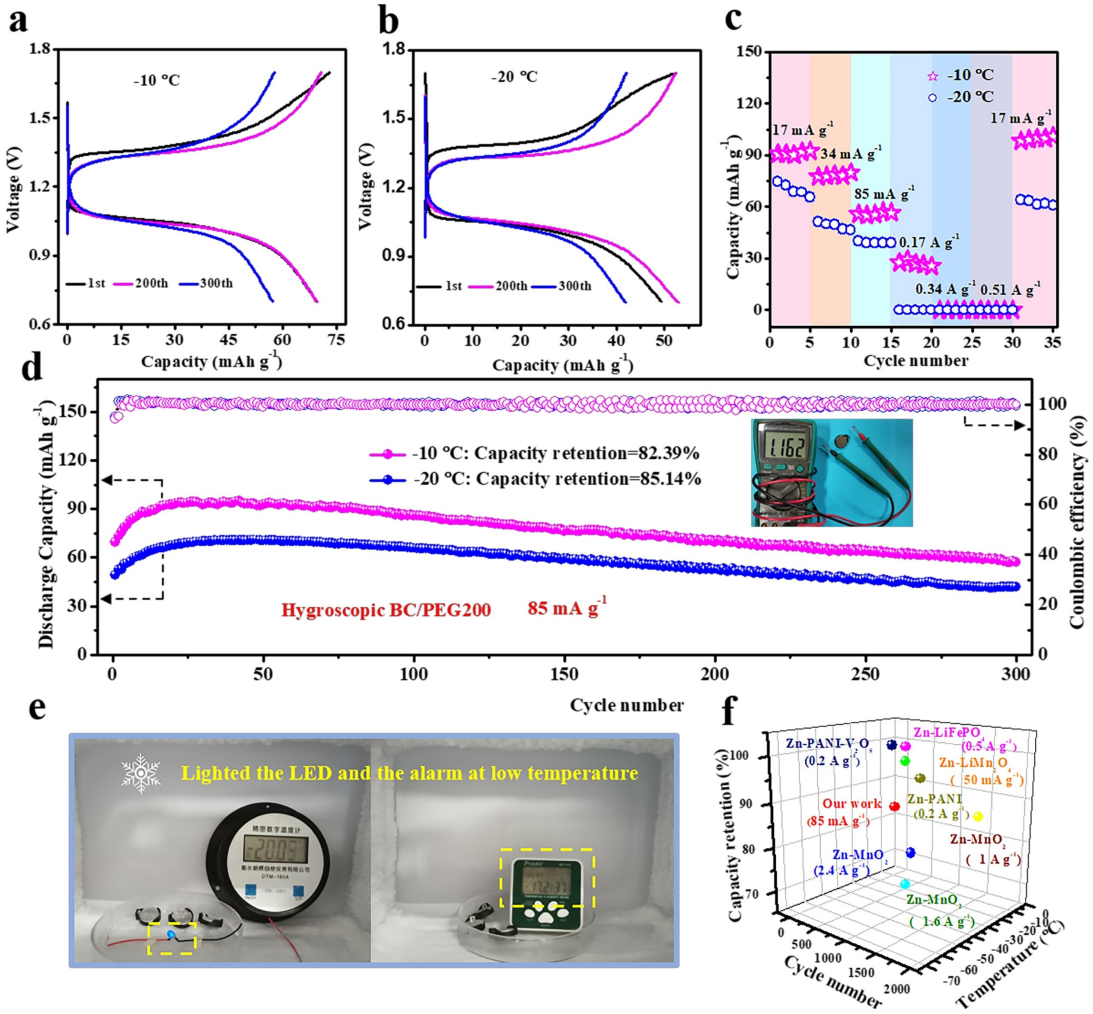

Figure 3. Electrochemical performances of Zn/LiFePO$_4$ batteries based on a hygroscopic double-layer gel polymer electrolyte at low temperatures. Charge–discharge curves of Zn/LiFePO$_4$ at a) −10 °C and b) −20 °C (85 mA g^{-1}). c) C-rate performance tested for Zn/LiFePO$_4$ batteries at low temperatures. d) Cycling stability of full cells with corresponding Coulombic efficiency at low temperatures and open circuit voltages of one battery (inset). e) The batteries continued to power the LED and alarm clock. f) Electrochemical performances comparison of our Zn/LiFePO$_4$ battery with other zinc batteries that can operate at low temperatures.

42.0 mAh g^{-1} after 300 cycles with a capacity retention and Coulombic efficiency of 85.14% and 100%, respectively. The theoretical specific capacity of the $LiFePO_4$ is 141 mAh g^{-1} according to the working mechanism of $LiFePO_4$/Zn battery. The capacity at −10 °C and −20 °C are much lower than the theoretical values mainly because of the poor electronic conductivity of $LiFePO_4$, low ion diffusion rate and large charge transfer resistance.[39,40] We also tested the cycle performance of batteries based on the hygroscopic PEG300 and PEG400 electrolytes (Figure S5, Supporting Information), with both still yielding capacity retentions above 70% after 300 cycles at −20 °C. Furthermore, the battery could be connected in series to light up an LED and power an alarm clock at low temperatures (Figure 3e). The Figure S2 shows the precipitation in the mixed acetonitrile solution (0.5 M $Zn(OTf)_2$ + 1 M LiTFSI). Therefore, A mixed acetonitrile solution with a low concentration of 0.2 M $Zn(OTf)_2$ + 0.4 M LiTFSI was used to prepare hygroscopic monolayer electrolyte. The hybrid battery based on hygroscopic monolayer electrolyte cannot work at −20 °C because of the freezing of electrolyte with low salt concentration, and corresponding ionic conductivity is 0.002 mS cm^{-1} (Figure S6, Supporting Information). The capacity retention of the battery based on hygroscopic monolayer electrolyte dropped to 52.07% only after 100 cycles at −10 °C. A study reported that a low current density will result in a faster capacity decay of aqueous zinc batteries than a high current density.[41] Compared with other zinc ion batteries that can operate at low temperatures, the battery rationally designed in this study has a more competitive cyclic stability at low current density (Figure 3f and Table S2, Supporting Information).

2.3. Critical Role of Water Molecules in Low-Temperature Zn/$LiFePO_4$ Batteries

A more intuitive explanation of the effect of water molecules on the above low-temperature hygroscopic gel electrolyte is that the ionic hydration reduces the freezing point of aqueous solutions by destructing H-bonds among the water molecules. Therefore, we exploited the frozen–thawed BC hydrogel as the supporting framework, and designed hydrogel electrolytes with varied $Zn(OTf)_2$ and LiTFSI concentrations ($C_{Zn(OTf)2+LiTFSI}$) for the Zn/$LiFePO_4$ hybrid battery, as shown in Figure S7a (Supporting Information). The "water-in-salt" term means that the mass and volume of the salt are higher than those of the water. In this study, we achieved this state using high salt concentrations of approximately 2 m $Zn(OTf)_2$ + 4 m LiTFSI (Figure S7b, Supporting Information). The evolution of H-bonds under different salt concentrations was explored by performing nuclear magnetic resonance (NMR), Fourier transform infrared spectroscopy (FTIR), and Raman spectroscopy. The analysis results are shown in Figure S8a–c (Supporting Information). The ^{1}H NMR spectra show that the ^{1}H peak of the pure water is located at 5.1 ppm. As the $C_{Zn(OTf)2+LiTFSI}$ increases, the ^{1}H peak shifts to the high field direction, and the signal gradually weakens, indicating the breakage of H-bonds. As for the FTIR spectra, pure water displays a wide band at 3200–3400 cm^{-1}, which is the typical O–H stretching vibration of water molecules. In comparison, the BC hydrogel shows a strong and narrow O–H stretching peak at 3342 cm^{-1}, demonstrating the new H-bonds formed between the cellulose and water molecules. When the salt concentration is maximized (2.5 m $Zn(OTf)_2$ + 5 m LiTFSI), the narrowing of the O–H peak is more noticeable. In addition, according to the Raman spectra, the strong H-bond peaks gradually weakened, with the weak H-bond peaks obtaining a blueshift as $C_{Zn(OTf)2+LiTFSI}$ increased.[19] In summary, at high concentrations, the H-bond structure among the water molecules was severely disturbed by the ionic hydration, which led to a decrease in the freezing point. As demonstrated by differential scanning calorimetry (DSC) in Figure S9 (Supporting Information), the freezing point of the pure BC hydrogel is −11.3 °C, which is a significantly lower freezing point than that of pure water. With the increase of $C_{Zn(OTf)2+LiTFSI}$, the freezing point of the hydrogel electrolyte increased to −20.5 °C, −46.5 °C, −97.6 °C, −97.8 °C and −15.1 °C in sequence.

As shown in Figure 4a, the pH of the double–salt aqueous solutions is weakly acidic, which is more favorable compared to alkaline electrolytes.[42] Having confirmed the excellent antifreeze properties of the BC hydrogel electrolyte, its electrochemical performance at low temperatures was studied. The ionic conductivity (σ) of the BC hydrogel electrolytes was obtained using electrochemical impedance spectroscopy (EIS) at different temperatures (Figure S10, Supporting Information). Compared to the σ at 25 °C, the hydrogel electrolyte possesses a much lower σ at −10 °C and −20 °C (Figure 4b). Among the various concentrations, the σ of the hydrogel electrolyte with 1.5 m $Zn(OTf)_2$ + 3 m LiTFSI exhibits a maximum of 1.20 mS cm^{-1} at −20 °C. Figure 4c shows perfectly symmetrical CV curves of a full cell, located between 0.7–1.7 V. The CV curves after five cycles at −20 °C maintained a more similar shape than at 25 °C, and the voltage between the oxidation peaks increased by ~120 mV. The polarization curves of the Zn/Zn symmetric cells with the BC hydrogel electrolyte were evaluated by cycling at a constant current density of 0.2 mA cm^{-2} for 500 h (Figure S11, Supporting Information). A polarization voltage reduction is observed at low temperatures, demonstrating a highly stable interface between the BC hydrogel and Zn anode, whereas the polarization voltage increased at 25 °C.

Figure 4d–f depicts the cycle performance of the full battery assembled with different $C_{Zn(OTf)2+LiTFSI}$ electrolytes at varying temperatures. For each salt concentration, the capacity retention after 100 cycles was shown to be less than 50% at 25 °C, but exceeded 50% at low temperatures. Specifically, for the salt concentration of 1.5 m $Zn(OTf)_2$ and 3 m LiTFSI, a capacity retention of approximately 83.15% was maintained at −20 °C. Although the activity of the cathode materials and σ degraded at low temperatures, the discharge specific capacity after ~10 cycles at −10 °C was already higher than that at room temperature. This phenomenon was verified by evaluating the cycle performance of the Zn/$LiFePO_4$ batteries based on the varied $C_{ZnSO4+LiTFSI}$ and $C_{ZnCl2+LiTFSI}$ electrolytes (Figure S12, 13, Supporting Information). Due to the low solubility of $ZnSO_4$ in water, the double–salt solutions froze at −20 °C. After testing,

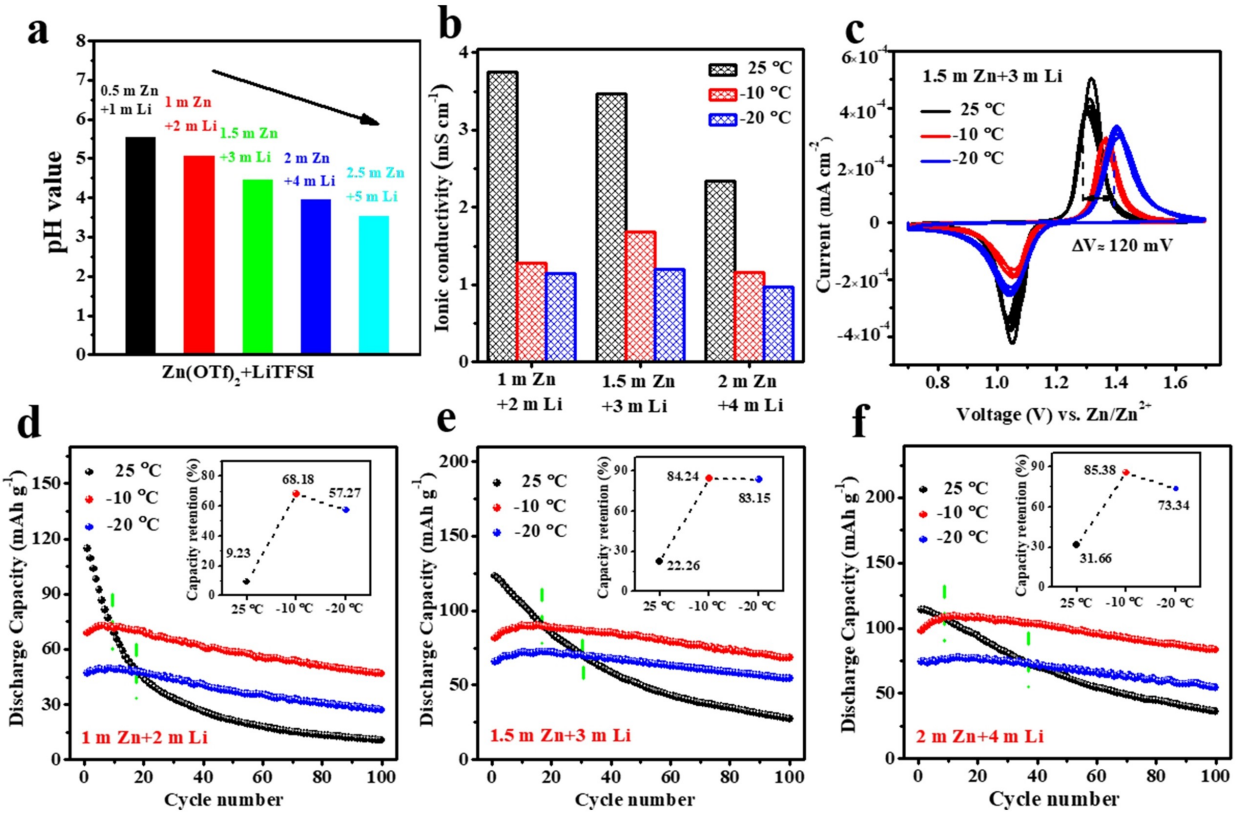

Figure 4. Critical role of water molecules in low-temperature Zn/$LiFePO_4$ batteries. a) The pH values of different $C_{Zn(OTf)2+LiTFSI}$ solutions. b) The σ of BC hydrogel electrolytes at different temperatures. c) CV curves of Zn/$LiFePO_4$ at a scan rate of 0.1 mV s^{-1} from 0.7 to 1.7 V. d–f) Cycling stability of Zn/$LiFePO_4$ batteries at varying temperatures (85 mA g^{-1}).

the capacity retention at 25 °C also reduced, particularly in the dilute electrolyte. As $ZnCl_2$ is one of the most soluble inorganic salts, there was no salting-out phenomenon at −20 °C even at a high salt concentration (2.5 m $ZnCl_2$ + 5 m LiTFSI). However, the Zn/$LiFePO_4$ batteries assembled based on different $C_{ZnCl2+LiTFSI}$ electrolytes all produced an OCV of ~0.8 V, which does not reach the theoretical value. Moreover, the charging voltage at 25 °C decreased sharply after reaching 1.2 V. It is believed that such a phenomenon is not caused by pH, because the pH of these solutions is similar for different $C_{Zn(OTf)2+LiTFSI}$ and $C_{ZnSO4+LiTFSI}$ solutions. This may be due to the chloride contained in the mixed electrolyte ($ZnCl_2$ + LiTFSI) causing severe corrosion to the stainless-steel current collector, thereby reducing the electronic conductivity and electrochemical window of the battery. Furthermore, further high-voltage charging will cause the oxidization and decomposition of the electrolyte at 1.2 V.[43,44] Surprisingly, the full cell based on the $C_{ZnCl2+LiTFSI}$ electrolyte (2.5 m $ZnCl_2$ + 5 m LiTFSI) achieved an impressive capacity retention of 98.53% after 100 cycles at −20 °C. The above results indicate that the aqueous zinc hybrid battery could obtain even better capacity retention in a low-temperature environment not stated in the present report.

2.4. Suppressed HER and OER in Hydrogel Electrolytes at Low Temperatures

To further unveil the unique mechanisms of aqueous Zn/$LiFePO_4$ batteries at low temperatures, we selected the BC hydrogel electrolyte of 1.5 m $Zn(OTf)_2$ + 3 m LiTFSI as the research object. The impedances of the full cells before and after 300 cycles were compared, as shown in Figure 5a and Figure S14 (Supporting Information). After 300 cycles at 25 °C, the charge transfer resistance (R_{ct}) of the full cell rose from 123 Ω to 2230 Ω. In contrast, when the temperature was further decreased to −20 °C, the R_{ct} only increased to 1058 Ω. This is likely because of the dehydration of the electrolyte or formation of by-products at room temperature. According to X-ray diffraction (XRD) analysis (Figure S15a, Supporting Information), owing to the high crystallinity of the metallic Zn, no other substances were observed on the surface of the Zn foil after cycling at different temperatures. However, the surface of the Zn foil cycled at 25 °C was found to be rough (Figure S15b–d, Supporting Information). The preceding results indicate that the temperature plays a prominent part in the electrochemical performance of the full battery with $ZnCl_2$ + LiTFSI electrolytes. We then disassembled the battery after charging for 13 h at 25 °C to examine the components (Figure S16, Supporting Information). Partial blackening of the zinc foil was observed and scanning electron microscopy (SEM) revealed a dense

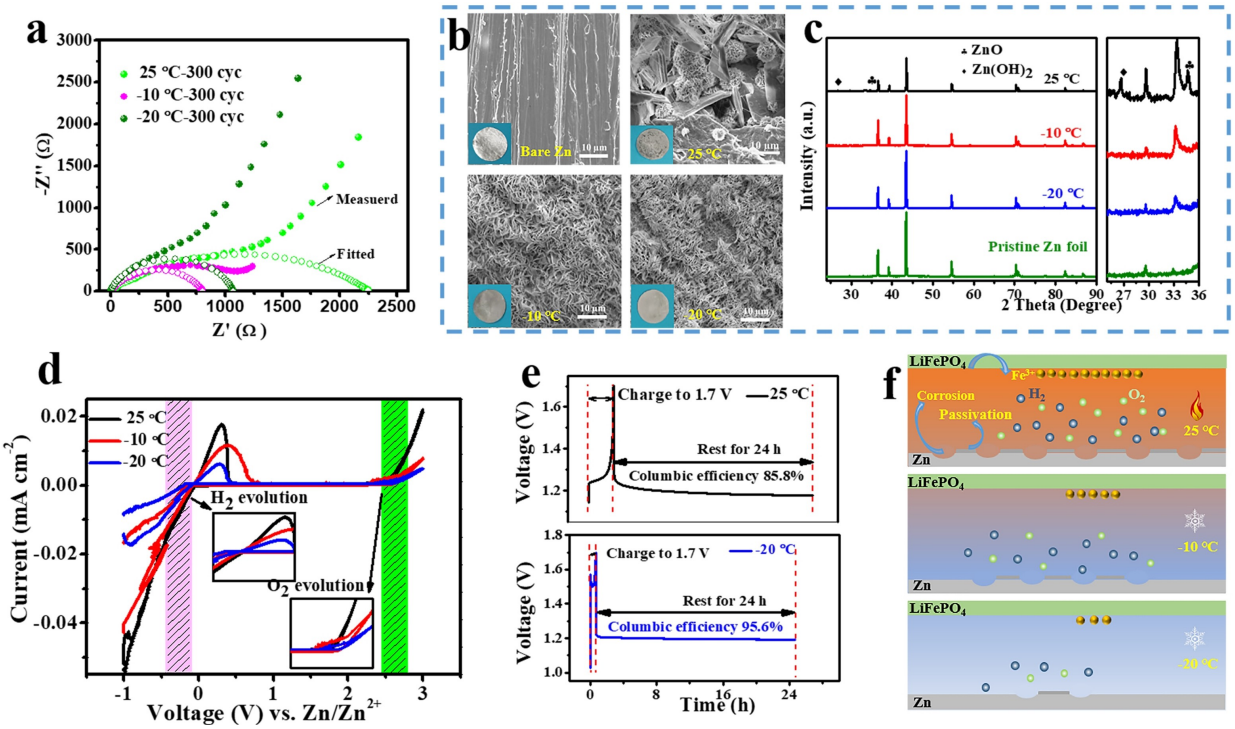

Figure 5. Suppressed HER and OER in hydrogel electrolytes at low temperatures. a) EIS plots of full cells after 300 cycles. b) SEM images and c) XRD patterns of bare Zn foil and Zn foil attached to BC hydrogel electrolytes for 10 days. d) CV curves of Zn plating/stripping using a three-electrodes test (stainless steel foil as a working electrode and Zn foil as reference and counter electrodes). e) Self-discharge curves of Zn/$LiFePO_4$ battery at 25 °C and −20 °C. f) Schematic illustration of Influence of temperature variation on anode corrosion and cathode dissolution.

formation of flakes and particles on the surface of the zinc foil. XRD spectra of the surface revealed that by-products of ZnO and $Zn(OH)_2$ had formed,, which was likely owing to the decomposition of the hydrates at 1.2 V during the charging process, leading to the formation of by-products. Furthermore, a side reaction was confirmed through SEM and XRD spectra of the commercial zinc foil, after it was attached to the hydrogel for 10 days at different temperatures (Figure 5b, c). The Zn foil at 25 °C severely corroded with a color change from bright metal to matte gray, and the surface was covered with flakes and velvety substances. Meanwhile, prominent peaks corresponding to ZnO and $Zn(OH)_2$ appeared in the XRD spectra. However, after cycling at lower temperatures, the cellulose layer on the surface of the Zn foil was difficult to remove, and no other substances were clearly visible on the surface.

We evaluated the electrochemical windows at different temperatures using a three-electrode configuration, as shown in Figure 5d. The electrochemical stability window of the electrolyte at 25 °C, relative to that of Zn/Zn^{2+}, was −0.11–2.34 V, while it widened to −0.19–2.58 V at −20 °C. These results indicate that the HER and OER can be attenuated at low temperatures. This parasitic reaction can also be evaluated by self-discharge curves of the full cell during standing (Figure 5e). Previous studies have shown that devices with intercalation energy storage have better anti-self-discharge ability than those with only ion adsorption energy storage (symmetrical supercapacitors).[45,46] In the absence of an electronic path, the self-diffusion of the ions fixed on the electrode is much slower than that of the ions adsorbed on the surface of the electrode. The zinc hybrid battery system in this work has excellent capacity retention at both 25 °C (85.8%) and −20 °C (95.6%) after 24 h. By contrast, the battery has more prominent anti-self-discharge ability at low temperatures. The OCV of the battery at −20 °C dropped from 1.7 V to 1.21 V after 0.1 h, as well as the subsequent fluctuation was almost negligible. However, the OCV at 25 °C has been dropping from 1.7 V to 1.17 V after 24 h.

In general, the OH^- and O_2 produced by the decomposition of water leads to the dissolution of active materials. In our case, we compared the morphology of $LiFePO_4$ cycled at different temperatures and found a negligible difference (Figure S17, Supporting Information). The composition and valence state of the $LiFePO_4$ cathode after 100 cycles were studied through X-ray photoelectron spectrometry (XPS), as shown in Figure S18 (Supporting Information). Compared to the $LiFePO_4$ cathode before cycling, the cycled $LiFePO_4$ cathodes have a stronger O 1s signal and weaker Li 1s, Fe 2p, P 2p, and C 1s signals. This phenomenon is more apparent at 25 °C. The intensity of the Fe 2p and C 1s signals reduced after cycling at 25 °C, which could be a result of Fe^{2+} dissolution and activated carbon separation from the cathode, leading to poor cycle life.[47] Based on the above analysis, the electrochemical data were confirmed. The corrosion of the Zn anode and dissolution of Fe^{2+} from $LiFePO_4$ due to HER and OER primarily caused a rapid capacity decay of the Zn/$LiFePO_4$ cell with hydrogel electrolytes

at ambient temperature (Figure 5f). This can be described by the following equations [Eqs. (1)–(3)]:

$$2\,H_2O + 2e^- \rightarrow H_2 \uparrow 2OH^- \quad (1)$$

$$Zn + 2\,OH^- \rightarrow ZnO + H_2O + 2\,e^- \quad (2)$$

$$2\,Fe^{2+} + O_2 + 2\,OH^- \rightarrow Fe_2O_3 + H_2O \quad (3)$$

Overall, developing a new strategy that exploits the low reactivity of water below 0 °C is a promising approach towards enhancing the cyclic stability of the zinc hybrid batteries.

3. Conclusion

In summary, by balancing the high costs caused by high salt concentrations, the "water-in-salt" electrolyte can be reversed to favor ion conduction by a hygroscopic double-layer BC/PEG electrolyte. A part of the interaction between the ether bond of PEG and the cation is converted into cation hydration, effectively inhibiting the decomposition of water while meeting the requirements of low-temperature operation. Another benefit is that a low-temperature environment can retard anode corrosion and cathode dissolution caused by water decomposition. In testing, the assembled cell presents an initial discharge specific capacity of 49.3 mAh g^{-1} at −20 °C. Moreover, nearly 85.14% of capacity is retained after 300 cycles with a Coulombic efficiency of ~100%. These results demonstrate the superiority of a small amount of water molecules at low-temperature in a zinc hybrid battery. This work encourages a pathway toward anti-freeze semisolid electrolytes for achieving high capacity, stability and security batteries with excellent adaptability at ultra-low temperature.

Acknowledgements

We acknowledge the financial support from the from the National Natural Science Foundation of China (NSFC) (Grant No. 21875055 and 21674031) and the Shenzhen Research Foundation Project (Grant GXWD20201230155427003)

Conflict of Interest

The authors declare no conflict of interest.

Keywords: bacterial cellulose · double-layer · hydrogels · low-temperature batteries · polyethylene glycol · zinc batteries

[1] J. M. Tarascon, M. Armand, *Nature* **2001**, *414*, 359–367.
[2] M. Armand, J. M. Tarascon, *Nature* **2008**, *451*, 652–657.
[3] Y. Liu, Y. Zhu, Y. Cui, *Nat. Energy* **2019**, *4*, 1.
[4] X. Zeng, M. Li, D. Abd El-Hady, W. Alshitari, A. S. Al-Bogami, J. Lu, K. Amine, *Adv. Energy Mater.* **2019**, *9*, 1900161.
[5] H. Li, L. Ma, C. Han, Z. Wang, Z. Liu, Z. Tang, C. Zhi, *Nano Energy* **2019**, *62*, 550–587.
[6] H. Jia, Z. Wang, B. Tawiah, Y. Wang, C.-Y. Chan, B. Fei, F. Pan, *Nano Energy* **2020**, *70*, 104523.
[7] Y. Tian, Y. An, C. Wei, B. Xi, S. Xiong, J. Feng, Y. Qian, *Adv. Energy Mater.* **2021**, *11*, 2002529.
[8] M. Cui, X. Bai, J. Zhu, C. Han, Y. Huang, L. Kang, C. Zhi, H. Li, *Energy Storage Mater.* **2021**, *36*, 427–434.
[9] B. Tang, L. Shan, S. Liang, J. Zhou, *Energy Environ. Sci.* **2019**, *12*, 3288–3304.
[10] J. Hao, X. Li, S. Zhang, F. Yang, X. Zeng, S. Zhang, G. Bo, C. Wang, Z. Guo, *Adv. Funct. Mater.* **2020**, *30*, 2001263.
[11] D. Han, S. Wu, S. Zhang, Y. Deng, C. Cui, L. Zhang, Y. Long, H. Li, Y. Tao, Z. Weng, Q.-H. Yang, F. Kang, *Small* **2020**, *16*, 2001736.
[12] M. Matsumoto, S. Saito, I. Ohmine, *Nature* **2002**, *416*, 409–413.
[13] J. Hao, X. Li, X. Zeng, D. Li, J. Mao, Z. Guo, *Energy Environ. Sci.* **2020**, *13*, 3917–3949.
[14] J. Hao, B. Li, X. Li, X. Zeng, S. Zhang, F. Yang, S. Liu, D. Li, C. Wu, Z. Guo, *Adv. Mater.* **2020**, *32*, 2003021.
[15] P. He, J.-L. Liu, W.-J. Cui, J.-Y. Luo, Y.-Y. Xia, *Electrochim. Act* **2011**, *56*, 2351–2357.
[16] H. Kim, J. Hong, K.-Y. Park, H. Kim, S.-W. Kim, K. Kang, *Chem. Rev.* **2014**, *114*, 11788–11827.
[17] F. Wang, O. Borodin, T. Gao, X. Fan, W. Sun, F. Han, A. Faraone, J. Dura, K. Xu, C. Wang, *Nat. Mater.* **2018**, *17*, 543.
[18] T. Liang, R. Hou, Q. Dou, H. Zhang, X. Yan, *Adv. Funct. Mater.* **2021**, *31*, 2006749.
[19] Q. Zhang, Y. Ma, Y. Lu, L. Li, F. Wan, K. Zhang, J. Chen, *Nat. Conmun.* **2020**, *11*, 4463.
[20] M. Zhu, X. Wang, H. Tang, J. Wang, Q. Hao, L. Liu, Y. Li, K. Zhang, O. G. Schmidt, *Adv. Funct. Mater.* **2020**, *30*, 1907218.
[21] L. Yang, L. Song, Y. Feng, M. Cao, P. Zhang, X.-F. Zhang, J. Yao, *J. Mater. Chem. A* **2020**, *8*, 12314–12318.
[22] L. Suo, O. Borodin, T. Gao, M. Olguin, J. Ho, X. Fan, C. Luo, C. Wang, K. Xu, *Science* **2015**, *350*, 938.
[23] C. Wang, Z. Pei, Q. Meng, C. Zhang, X. Sui, Z. Yuan, S. Wang, Y. Chen, *Angew. Chem. Int. Ed.* **2021**, *60*, 990–997; *Angew. Chem.* **2021**, *133*, 1003–1010.
[24] D. Kundu, S. Hosseini Vajargah, L. Wan, B. Adams, D. Prendergast, L. F. Nazar, *Energy Environ. Sci.* **2018**, *11*, 881–892.
[25] H. Zhang, X. Wu, T. Yang, S. Liang, X. Yang, *Chem. Commun.* **2013**, *49*, 9977–9979.
[26] X. Zeng, J. Hao, Z. Wang, J. Mao, Z. Guo, *Energy Storage Mater.* **2019**, *20*, 410–437.
[27] A. Nakayama, A. Kakugo, J. P. Gong, Y. Osada, M. Takai, T. Erata, S. Kawano, *Adv. Funct. Mater.* **2004**, *14*, 1124–1128.
[28] C. Ding, X. Fu, H. Li, J. Yang, J.-L. Lan, Y. Yu, W.-H. Zhong, X. Yang, *Adv. Funct. Mater.* **2019**, *29*, 1904547.
[29] J. Wu, Z. Rao, Z. Cheng, L. Yuan, Z. Li, Y. Huang, *Adv. Energy Mater.* **2019**, *9*, 1902767.
[30] C.-y. Yan, Z.-q. Fang, A.-m. Tang, W.-y. Liu, Y. Liu, H.-z. Shi, *Cellulose* **2018**, *25*, 2405–2417.
[31] S. Huang, F. Wan, S. Bi, J. Zhu, Z. Niu, J. Chen, *Angew. Chem. Int. Ed.* **2019**, *58*, 4313–4317; *Angew. Chem.* **2019**, *131*, 4357–4361.
[32] H. Bi, X. Wang, H. Liu, Y. He, W. Wang, W. Deng, X. Ma, Y. Wang, W. Rao, Y. Chai, H. Ma, R. Li, J. Chen, Y. Wang, M. Xue, *Adv. Mater.* **2020**, *32*, 2000074.
[33] L. Chen, J. Zhang, Q. Li, J. Vatamanu, C. Wang, *ACS Energy Lett.* **2020**, *5*, 968–974.
[34] Q. Dou, Y. Lu, L. Su, X. Zhang, S. Lei, X. Bu, L. Liu, D. Xiao, J. Chen, S. Shi, X. Yan, *Energy Storage Mater.* **2019**, *23*, 603–609.
[35] S. Xiao, J. Nie, R. Tan, X. Duan, J. Ma, Q. Li, T. Wang, *Mater. Chem. Front.* **2019**, *3*, 484–491.
[36] S. Xu, Z. Sun, C. Sun, F. Li, K. Chen, Z. Zhang, G. Hou, H.-M. Cheng, F. Li, *Adv. Funct. Mater.* **2020**, *30*, 2007172.
[37] B. M. Savoie, M. A. Webb, T. F. Miller, *J. Phys. Chem. Lett.* **2017**, *8*, 641–646.
[38] D. Lin, P. Y. Yuen, Y. Liu, W. Liu, N. Liu, R. H. Dauskardt, Y. Cui, *Adv. Mater.* **2018**, *30*, 1802661.
[39] J. Hou, M. Yang, D. Wang, J. Zhang, *Adv. Energy Mater.* **2020**, *10*, 1904152.
[40] A. Ramanujapuram, G. Yushin, *Adv. Energy Mater.* **2018**, *8*, 1802624.
[41] L. Zhang, I. A. Rodríguez-Pérez, H. Jiang, C. Zhang, D. P. Leonard, Q. Guo, W. Wang, S. Han, L. Wang, X. Ji, *Adv. Funct. Mater.* **2019**, *29*, 1902653.

[42] Y. Li, J. Fu, C. Zhong, T. Wu, Z. Chen, W. Hu, K. Amine, J. Lu, *Adv. Energy Mater.* **2019**, *9*, 1802605.
[43] C. Wall, Z. Zhao-Karger, M. Fichtner, *ECS Electrochem. Lett.* **2014**, *4*, C8–C10.
[44] S. Yagi, A. Tanaka, Y. Ichikawa, T. Ichitsubo, E. Matsubara, *J. Electrochem. Soc.* **2013**, *160*, C83–C88.
[45] Z. Huang, A. Chen, F. Mo, G. Liang, X. Li, Q. Yang, Y. Guo, Z. Chen, Q. Li, B. Dong, C. Zhi, *Adv. Energy Mater.* **2020**, *10*, 2001024.
[46] Z. Huang, T. Wang, H. Song, X. Li, G. Liang, D. Wang, Q. Yang, Z. Chen, L. Ma, Z. Liu, B. Gao, J. Fan, C. Zhi, *Angew. Chem. Int. Ed.* **2021**, *60*, 1011–1021; *Angew. Chem.* **2021**, *133*, 1024–1034.
[47] D. Gordon, M. Y. Wu, A. Ramanujapuram, J. Benson, J. T. Lee, A. Magasinski, N. Nitta, C. Huang, G. Yushin, *Adv. Energy Mater.* **2016**, *6*, 1501805.

Manuscript received: May 26, 2021
Revised manuscript received: June 21, 2021
Version of record online: July 20, 2021